Acta Oceanol. Sin., 2025, Vol. 44, No. 3, P. 130–146
https://doi.org/10.1007/s13131-025-2478-0

Energetics of eddy-mean flow interactions in the Ross Sea

Kechen Liu[1], Chengyan Liu[2*], Zhaomin Wang[2], Liangjun Yan[3], Yang Wu[4], Yang Liu[1], Yue Xia[1], Xi Liang[5], Xiang Li[2], Wen Xu[6]

[1] School of Atmospheric Sciences, Sun Yat-sen University, Zhuhai 519082, China

[2] Southern Marine Science and Engineering Guangdong Laboratory (Zhuhai), Zhuhai 519082, China

[3] School of Marine Science, Sun Yat-sen University, Zhuhai 519082, China

[4] School of Information Engineering, Nanjing Xiaozhuang University, Nanjing 211171, China

[5] Key Laboratory of Marine Hazards Forecasting, National Marine Environmental Forecasting Center, Ministry of Natural Resources, Beijing 100081, China

[6] Ocean Academy, Ocean College, Zhejiang University, Zhoushan 316021, China

Received 31 August 2024; accepted 18 April 2025

© Chinese Society for Oceanography and Springer-Verlag GmbH Germany, part of Springer Nature 2025

Abstract

The oceanic general circulations in the Ross Sea, where the southernmost ocean is located, play an important role in the climate system. Yet, the energy cycle of oceanic circulations in the Ross Sea is still unclear. By employing an eddy-permitting coupled regional ocean-sea ice-ice shelf model, this study investigates the oceanic energy cycle in the Ross Sea. Based on the Lorenz Energy Cycle framework, the spatiotemporal distributions of kinetic energy and available potential energy within the Ross Sea are quantitatively analyzed. The power pathways and magnitudes of energy conversion are also quantified. The simulated results show that the Mean Available Potential Energy (MAPE) is the largest energy reservoir of about 527.62 PJ (1 PJ = 10^{15} J), followed by the Eddy Available Potential Energy (EAPE), the Mean Kinetic Energy (MKE), and the Eddy Kinetic Energy (EKE) of about 19.20 PJ, 1.04 PJ, and 0.82 PJ, respectively. In the sub-ice-shelf cavity, the maximal MAPE is up to about 177.81 PJ, and the EAPE, MKE, and EKE are about 2.58 PJ, 39.87 TJ (1 TJ = 10^{12} J), and 23.05 TJ, respectively. The inputs to the regional energy reservoirs are mainly from the sea surface momentum and buoyancy fluxes. The baroclinic pathway plays a dominant role in the conversion of energy to EKE, both in the open ocean and in the sub-ice-shelf cavity. The energy conversion from EAPE to EKE in the open ocean and the sub-ice-shelf cavity is about 2.86 GW (1 GW = 10^9 J) and 162.18 MW(1 MW = 10^6 J), respectively. In addition, the kinetic energy is directed from EKE to MKE in the Ross Sea, and such an energy flow in the barotropic pathway is opposite from that in the Southern Ocean.

Key words Ross Sea, Lorenz Energy Cycle, kinetic energy, available potential energy, Ross Ice Shelf, regional model

Citation Liu Kechen, Liu Chengyan, Wang Zhaomin, Yan Liangjun, Wu Yang, Liu Yang, Xia Yue, Liang Xi, Li Xiang, Xu Wen. 2025. Energetics of eddy-mean flow interactions in the Ross Sea. Acta Oceanologica Sinica, 44(3): 130–146, doi: 10.1007/s13131-025-2478-0

1 Introduction

Quantitative descriptions of the oceanic energy cycle can enhance our understanding of oceanic circulation dynamics. The Lorenz Energy Cycle (LEC) has been recognized as a useful research method for investigating both atmospheric and oceanic circulations (Lorenz, 1955; Oort and Peixóto, 1983). Oort et al. (1994) computed energy budgets using ocean surface observations, encompassing terms for energy generation, conversion, and dissipation. Wunsch and Ferrari (2004) estimated major energy reservoirs and transfers toward dissipation in the global ocean,

Foundation item: The Independent Research Foundation of Southern Marine Science and Engineering Guangdong Laboratory (Zhuhai) under contract No. SML2023SP201; the Natural Science Foundation of Guangdong Province, China under contract No. 2024A1515012717; the Funds of Southern Marine Science and Engineering Guangdong Laboratory (Zhuhai) under contract Nos 313021004 and 313022009; the National Natural Science Foundation of China under contract No. 41806216; the Natural Science Foundation of Jiangsu Province under contract No. BK20211015; the Program of Innovation 2030 on Smart Ocean, Zhejiang University.

*Corresponding author, E-mail: liuchengyan@sml-zhuhai.cn

and then Ferrari and Wunsch (2009, 2010) put forward an updated energy budget framework that is focused on the Kinetic Energy (KE) of oceanic circulations. Tailleux (2009) proposed a framework of Available Potential Energy (APE) based on the fully compressible Navier-Stokes equations, and Tailleux (2010) highlighted the influences of buoyancy power input on the oceanic energy cycle. Yet, Huang (2004) proposed that the mechanical energy input of wind stress plays a more important role in driving oceanic circulations, although an accurate definition of APE remains a challenge (Huang, 2005).

Previous observational studies have greatly improved our understanding of the Ross Sea and provided an amount of hydrography observations, including *in-situ* observations from moorings, equipment seals, borehole sites, voyages and flights, and remote sensing from satellites (Castagno et al., 2017, 2019; Biddle and Swart, 2020; Stevens et al., 2020; Rack et al., 2021). However, mooring and borehole observations deployed at fixed stations cannot provide data with a broad spatial extension, and measurements from seals and voyages cannot provide data with long-term periods. Satellite observations mainly measure the surface layer of the ocean. Therefore, previous studies tended to explore the oceanic energy cycle with the aid of numerical models (Cox, 1985; Olbers et al., 2012; von Storch et al., 2012; Chen et al., 2014; Kang and Curchitser, 2015; Wu et al., 2017; Jüling et al., 2018). By utilizing a global simulation with a resolution of about 0.1°, von Storch et al. (2012) found that the global energy generation rates are about 6.6 TW, with about 4.0 TW and 2.6 TW attributed to wind stress and buoyancy flux, respectively. The global energy dissipation rates are about 4.4 TW and 2.3 TW attributed to KE dissipation and APE dissipation, respectively (von Storch et al., 2012). Ssebandeke et al. (2024) examined the sensitivity of global LEC to different atmospheric forcing, and they suggested that the Eddy Kinetic Energy (EKE) is insensitive to elevated wind stress due to the enhanced dissipation at the sea surface. Based on the Estimating the Circulation and Climate of the Ocean, phase 2, high-resolution global-ocean and sea ice data synthesis (ECCO2; Menemenlis et al., 2008) state estimate (18 km resolution), Chen et al. (2014) found that the energy conversion between KE and APE in the subtropical region is much weaker than in the Southern Ocean. By conducting sensitivity experiments with ECCO2, Wu et al. (2017) examined the impacts of intensified westerlies on the LEC in the Southern Ocean, and Wu et al. (2017) identified significant increases in energy reservoirs and enhanced energy conversions over significant topographic features when the ocean is driven by intensified westerlies. Furthermore, by using the simulated results from the ocean general circulation model for the Earth Simulator (0.1°; Masumoto et al., 2004), Matsuta and Masumoto (2023) also highlighted that standing meanders associated with significant topographic features are responsible for the pronounced energy transfer among reservoirs downstream.

In contrast to the oceanic energetics at lower latitudes, the oceanic energy cycle in the Antarctic marginal seas may have substantially different characteristics due to the vigorous atmospheric forcing, the sea ice evolution, and the existence of ice shelves. Due to gravity, cold air above the Antarctic Ice Sheet can converge and descend to the sea surface in the austral winter, with wind speed often exceeding 20 m/s and air temperature below −25℃ (Thompson et al., 2020). Such strong and cold atmospheric forcing is expected to induce drastic air-sea momentum and heat flux and the production of sea ice. The sea ice plays an important role in insulating the underlying ocean from the atmosphere, suppressing air-sea exchange fluxes in winter. Yet, the katabatic winds around the Antarctic margins can blow sea ice offshore to form polynyas that are the opening areas with low sea ice concentration in winter. Therefore, air-sea momentum and heat flux are still remarkable within polynyas, with very high sea ice production (Tamura and Ohshima, 2011; Tamura et al., 2011). Ice shelves are thick masses of floating ice fed by land glaciers extending from the land into the ocean. Generally, the ice temperature at the basal surface of ice shelves is much lower than the sea surface freezing point (Herraiz-Borreguero et al., 2013), and thereby profound fresh water and heat exchanges can occur at the ocean-ice shelf interface in the sub-ice-shelf cavity (Rignot et al., 2013). Accordingly, the generations of KE and APE in the Antarctic marginal seas are expected to be substantially different from those at lower latitudes.

Apart from the studies focused on the energy cycles in global ocean basins, a detailed description of oceanic energetics around the Antarctic marginal seas can improve our understanding of the complex climate system in polar regions. On the one hand, due to logistical challenges, field observations are insufficient to study the LEC over the Antarctic marginal regions directly. On the other hand, global general circulation models with relatively coarse resolutions may not be able to properly simulate the EKE over the Antarctic shelf seas at such higher latitudes. Therefore, it is necessary to study the LEC over the Antarctic marginal seas with the aid of a high-resolution regional coupled ocean-sea ice-ice shelf model. So far, Wu et al. (2021) are the first to study the LEC in the sub-ice-shelf cavity of the Amery Ice Shelf in Prydz Bay, East Antarctica. To our knowledge, this study is the first to analyze the energetics of eddy-mean flow interactions in the Ross Sea and the cavity beneath the Ross Ice Shelf (RIS), which is the largest ice shelf in the world. As such, an investigation of the LEC in the Ross Sea could provide insights into our understanding of the complex oceanic circulations around Antarctica and their corresponding influences.

The organization of this paper is as follows. Section 2 provides a brief description of the model configuration. Section 3 outlines the definitions of four energy reservoirs, along with the derivation of energy generation, con-

version, and boundary flux. Based on Section 3, Sections 4–6 present the analysis of the energy reservoirs and corresponding generation and conversion terms. Section 7 provides an overall picture of LEC in the Ross Sea and the sub-ice-shelf cavity. Section 8 gives the summary and concluding remarks. Some details are provided in the supplementary imformation (Figs S1−S36).

2 Model description

The Massachusetts Institute of Technology general circulation model (MITgcm) (Marshall et al., 1997a, 1997b) is used to configure a coupled regional ocean-sea-ice-shelf model for the Ross Sea (Yan et al., 2023). The MITgcm is based on the Navier-Stokes equations with the Boussinesq approximation, and this regional model adopts the hydrostatic assumption. A dynamic and thermodynamic sea ice model (Zhang and Hibler III, 1997; Zhang and Rothrock, 2000) and a thermodynamic ice shelf model (Losch et al., 2010) are coupled to the ocean model.

Figure 1 shows the model domain that includes the deep ocean and the continental shelf in the Ross Sea and the RIS, with a uniform horizontal resolution of about 5 km × 5 km (Fig. 1b). It is worth noting that such a high-resolution horizontal grid spacing may still not be able to fully resolve mesoscale eddies over the continental shelf where the first baroclinic Rossby deformation radius could be only a few kilometers (see Fig. S30). The first baroclinic Rossby deformation radius is the length scale of baroclinic variability longer than which the internal vortex stretching would be more important than the relative vorticity (Chelton et al., 1998). Therefore, it is expected that this coupled regional ocean-sea ice-shelf model is still an eddy-permitting model, and it may underestimate corresponding mixing and heat and salt transport. The vertical layers have 70 unevenly spaced intervals, with the layer thickness ranging from 10 m at the surface to 600 m at the sea floor (Fig. 1c). The partial cell is used to improve the representation of topography that is adopted from the Refined Topography Data Set 2 (RTopo-2; Schaffer et al., 2016) to represent the depth of the seafloor and the geometry of sub-ice-shelf cavities. RTopo-2 is a combined bathymetric data set based on the International Bathymetric Chart of the Southern Ocean (IBCSO; Arndt et al., 2013) and the Bedmap-2 (Fretwell et al., 2013), with a resolution of 500 m. The IBCSO complies with the bathymetric data from single-beam/multibeam echo sounding and digitized depths from nautical charts (Arndt et al., 2013). Bedmap-2 incorporates bathymetric data from satellite observations, airborne radar surveys, over-snow radar, and seismic sounding data (Fretwell et al., 2013). However, since there is still an amount of data gaps in the *in-situ* observations that are used to construct IBCSO and Bedmap-2 (Fretwell et al., 2013), uncertainties in the RTopo-2 may still be relatively large (Sun et al., 2022).

The open boundary conditions, including the velocities, temperatures, and salinity, are derived from the Southern Ocean State Estimate (Mazloff et al., 2010; Verdy and Mazloff, 2017) and the World Ocean Atlas 2018 (WOA18, Locarnini et al., 2019; Zweng et al., 2019). Tidal forcing on the open boundaries, including 10 major tidal constituents, is derived from the Circum-Antarctic Tidal Simulation (Padman et al., 2002, 2003, 2009). The open boundary conditions of the sea ice, including snow thickness, sea ice thickness, sea ice concentration, and sea ice velocity, are obtained from the Southern Ocean State Estimate and the National Snow and Ice Data Center (Fetterer et al., 2017). Since the open boundary conditions may increase the uncertainties of our analysis, we only conduct the LEC analysis within the selected region shown in Fig. 1 rather than the entire model domain (the inset of Fig. 1). In addition, the LEC in the RIS cavity has also been analyzed separately.

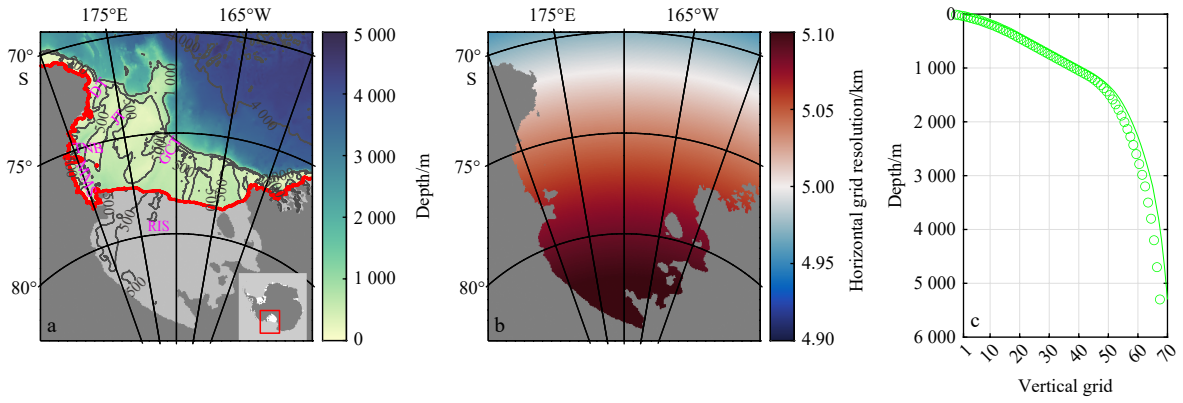


Fig. 1. Focused region of the LEC analysis in this study (a), the horizontal grid resolution (b), and the vertical grid configuration (c). In a, the red box in the inset shows the entire model domain; the color shading represents the topographic features of the Ross Sea; the red line shows the coastline and the ice shelf calving front; the grey region denotes the land, and the semitransparent region denotes the ice shelves region; the thin grey lines represent the 500 m, 1 000 m, and 4 000 m isobaths; DT, Drygalski Trough; JT, Joides Trough; GCT, Glomar Challenger Trough; MMS, McMurdo Sound; RIS, Ross Ice Shelf; TNB, Terra Nova Bay.

The model employs the European Centre for Medium-Range Weather Forecasts Reanalysis v5 as the atmospheric forcing (Hersbach et al., 2020), with a temporal resolution of 1 h and a spatial resolution of 0.25° × 0.25°. The model is initialized when the ocean is at rest. The initial conditions of potential temperature and salinity are horizontally uniform vertical profiles. The values of the vertical profiles are derived from the area-averaged values of WOA18 within the model domain. The model integration ranges from 1979 to 2015, and the daily model outputs in the last ten years are saved for the LEC analysis in this study. The model configuration and model validation have been described in Yan et al. (2023) in details, and the simulated velocity (associated with KE) and potential density (associated with APE) have been further compared with hydrographic observations to assess the ability of the model for the LEC analysis in this study (see Figs S1−S25 for the details).

3 Terms of the LEC framework

There are four energy reservoirs in the LEC, including Mean Kinetic Energy (MKE, K_m), EKE (K_e), Mean Available Potential Energy (MAPE, P_m), and Eddy Available Potential Energy (EAPE, P_e). The seasonal cycle in the Antarctic marginal seas is so strong that it can exert a strong influence on the calculation of K_e and P_e. Since we are very interested in the long-term mean state of oceanic energy and the mesoscale variability. So, in this study, the time-mean components refer to the temporal average over the last ten years (2005–2015), and the time-varying components are the deviation of model daily outputs from the time mean.

The MKE and EKE are as follows:

$$K_\mathrm{m} = \int_V \frac{1}{2}\rho_0\left(\overline{u}^2 + \overline{v}^2\right)\mathrm{d}V, \tag{1}$$

$$K_\mathrm{e} = \int_V \frac{1}{2}\rho_0\left(\overline{u'^2 + v'^2}\right)\mathrm{d}V, \tag{2}$$

where ρ_0 is a constant reference density (1 038 kg/m^3), u is the zonal velocity, and v is the meridional velocity. The overbar denotes the time mean (2005–2015), and the prime denotes the deviation from the time-mean value. Hereafter, the subscript V is the volume of the interested region in the Ross Sea (Fig. 1a). Following von Storch et al. (2012), P_m and P_e are defined as follows:

$$P_\mathrm{m} = -\int_V \frac{g}{2n_0}\overline{\rho^{*2}}\mathrm{d}V, \tag{3}$$

$$P_\mathrm{e} = -\int_V \frac{g}{2n_0}\overline{\rho'^2}\mathrm{d}V, \tag{4}$$

where $g = 9.8$ m/s^2 is the gravitational acceleration, and n_0 represents the vertical gradient of the time and area mean of local potential density. ρ is the local density, $\rho^*(x, y, z, t) = \rho(x, y, z, t) - <\overline{\rho(x, y, z, t)}>$, and $<\cdot>$ represents the area mean at a given depth. $<\overline{\rho(x, y, z, t)}>$ is the reference density defined by the area average (Fig. 1) of the time-mean density.

The oceanic energy budget equations are as follows (von Storch et al., 2012):

$$\frac{\mathrm{d}K_\mathrm{m}}{\mathrm{d}t} = G(K_\mathrm{m}) + C(K_\mathrm{e}, K_\mathrm{m}) + C(P_\mathrm{m}, K_\mathrm{m}) + B(K_\mathrm{m}) - D(K_\mathrm{m}), \tag{5}$$

$$\frac{\mathrm{d}K_\mathrm{e}}{\mathrm{d}t} = G(K_\mathrm{e}) - C(K_\mathrm{e}, K_\mathrm{m}) + C(P_\mathrm{e}, K_\mathrm{e}) + B(K_\mathrm{e}) - D(K_\mathrm{e}), \tag{6}$$

$$\frac{\mathrm{d}P_\mathrm{m}}{\mathrm{d}t} = G(P_\mathrm{m}) + C(P_\mathrm{e}, P_\mathrm{m}) - C(P_\mathrm{m}, K_\mathrm{m}) + B(P_\mathrm{m}) - D(P_\mathrm{m}), \tag{7}$$

$$\frac{\mathrm{d}P_\mathrm{e}}{\mathrm{d}t} = G(P_\mathrm{e}) - C(P_\mathrm{e}, P_\mathrm{m}) - C(P_\mathrm{e}, K_\mathrm{e}) + B(P_\mathrm{e}) - D(P_\mathrm{e}), \tag{8}$$

where G represents the generation terms, C represents the conversion terms, B represents the boundary flux terms, and D represents the dissipation terms.

$G(K_\mathrm{m})$ and $G(K_\mathrm{e})$ denote the generation terms of MKE and EKE, induced by time-mean wind stress and time-varying wind stress, respectively. When the direction of the wind is the same as the orientation of the current, the wind tends to export power to the ocean, and vice versa. $G(P_\mathrm{m})$ and $G(P_\mathrm{e})$ denote the generation terms of MAPE and EAPE induced by the surface buoyancy fluxes, respectively. Adding (extracting) freshwater to (from) relatively light (heavy) water masses can result in the generation of APE, and so does by heating (cooling) relatively light (heavy) water masses.

The rates of generation terms are as follows:

$$G(K_\mathrm{m}) = \int_s \left(\overline{\tau_{x,\mathrm{s}}}\,\overline{u_\mathrm{s}} + \overline{\tau_{y,\mathrm{s}}}\,\overline{v_\mathrm{s}}\right)\mathrm{d}S, \tag{9}$$

$$G(K_\mathrm{e}) = \int_s \left(\overline{\tau_{x,}u_{s'}} + \overline{\tau'_{y,\mathrm{s}}v'_\mathrm{s}}\right)\mathrm{d}S, \tag{10}$$

$$G(P_\mathrm{m}) = -\int_s \frac{\overline{\rho^*}}{n_0}\overline{B_0}\mathrm{d}S, \tag{11}$$

$$G(P_\mathrm{e}) = -\int_s \overline{\frac{\rho'}{n_0}B'_0}\mathrm{d}S, \tag{12}$$

where $\tau_{x,\mathrm{s}}$ and $\tau_{y,\mathrm{s}}$ are the surface wind stress, and u_s and v_s denote the ocean surface velocity. $B_0 = \frac{g}{\rho_0}\left(\frac{\alpha Q^*}{C_w} + \rho_0\beta S E^*\right)$, and α and β are the temperature and salinity expansion coefficients, respectively. C_w denotes the heat capacity of seawater, and S denotes the salinity. Q^* is the net air-sea heat flux, and E^* is the net air-sea freshwater flux.

The conversion terms are given by

$$C(K_\mathrm{e}, K_\mathrm{m}) = \int_V \left(\rho_0\overline{\boldsymbol{u'u'}}\cdot\nabla\overline{u} + \rho_0\overline{\boldsymbol{v'u'}}\cdot\nabla\overline{v}\right)\mathrm{d}V, \tag{13}$$

$$C(P_e,K_e) = -\int_V g\overline{\rho' w'}\mathrm{d}V, \tag{14}$$

$$C(P_m,K_m) = -\int_V g\overline{\rho^*}\overline{w}\mathrm{d}V, \tag{15}$$

$$C(P_e,P_m) = -\int_V \frac{g}{n_0}\overline{\rho' \boldsymbol{u}'_h}\cdot\nabla_h\overline{\rho^*}\mathrm{d}V, \tag{16}$$

where ∇_h is the horizontal nabla operator, w denotes the vertical velocity, $\boldsymbol{u}$ and $\boldsymbol{u}_h$ are three-dimensional and horizontal velocity vector. $C(X,Y)$ represents conversion rate from X to Y, and $C(X,Y) = -C(Y,X)$.

On open boundaries of the interested domain, energy flux arises from the advection of water masses and pressure work (Jüling et al., 2018). The boundary fluxes terms are given by

$$B(K_m) = \oint_{\Omega^s}\left(\overline{\boldsymbol{u}_h}K_m + \overline{\boldsymbol{u}_h}\overline{P^*}\right)\cdot\boldsymbol{n}\mathrm{d}\Omega^s, \tag{17}$$

$$B(K_e) = \oint_{\Omega^s}\left(\overline{(\boldsymbol{u}_h\frac{1}{2}\rho_0(u'^2+v'^2))} + \overline{\boldsymbol{u}'_h P'}\right)\cdot\boldsymbol{n}\mathrm{d}\Omega^s, \tag{18}$$

$$B(P_m) = \oint_{\Omega^s}(\overline{\boldsymbol{u}_h}P_m)\cdot\boldsymbol{n}\mathrm{d}\Omega^s, \tag{19}$$

$$B(P_e) = \oint_{\Omega^s}(-\overline{\boldsymbol{u}_h P_e})\cdot\boldsymbol{n}\mathrm{d}\Omega^s, \tag{20}$$

where $P^*(x,y,z,t) = P(x,y,z,t) - <\overline{P(z)}>$, and $<\overline{P(z)}>$ is the area average of the time-mean hydrostatic reference pressure, $\boldsymbol{n}$ denotes the unit normal vector of the boundary surface Ω, and Ω^s represents the area of the boundary surface.

The dissipation terms $D(K_m)$, $D(K_e)$, $D(P_m)$, and $D(P_e)$ are computed as the residual from the corresponding Eqs (5)–(8), respectively. Therefore, the LEC analysis here represents an approximate balance.

The open ocean is influenced by the atmospheric forcing and the sea ice evolution, while the ocean in the sub-ice-shelf cavity is isolated from the atmosphere, and hence we conduct the LEC analysis over the open ocean and in the RIS cavity, respectively.

4 Energy reservoirs

According to Eqs (1)−(4), we calculated the terms of energy reservoirs K_m, K_e, P_e, and P_m.

Figure 2 clearly shows that depth-averaged energy densities of K_m and K_e exhibit distinctly different spatial distributions. The large value of K_m is confined within narrow filaments (Fig. 2a), implying that the paths of the time-mean currents are consistent over time. In contrast, K_e reveals a much smoother spatial pattern than the K_m (Fig. 2b), implying that the spatial positions of time-varying flows often change.

For the time-mean circulations (Fig. 2a), K_m, strong KE are concentrated along the calving front of the RIS, the submarine troughs (the deep seabed enclosed by the 500 m isobaths in the Ross Sea), and the continental slope. Large values of K_m on the continental shelf are along the 500 m isobaths that are the bounds of submarine troughs, and strong K_m along the coastal lines and the continental slope also fluctuate with the spatial position of the RIS front and the 1 000 m isobaths. Such a spatial pattern of K_m implies that the temporal averaged circulations should be mainly dominated by the topography. The maximal value of K_m is identified over the northwestern continental slope where the dense shelf water overflows from the continental shelf into the deep ocean to form Antarctic Bottom Water. The value of K_m in the western and middle flanks of the RIS cavity is larger than in the eastern flank (Fig. 2a). Since K_m is mainly concentrated in the relatively stable oceanic circulations, the distribution of KE in the RIS cavity also reflects that the predominant gyres are determined by the geometry of the sub-ice-shelf cavity and the effects of “ice pump” (Lewis, 1985), which

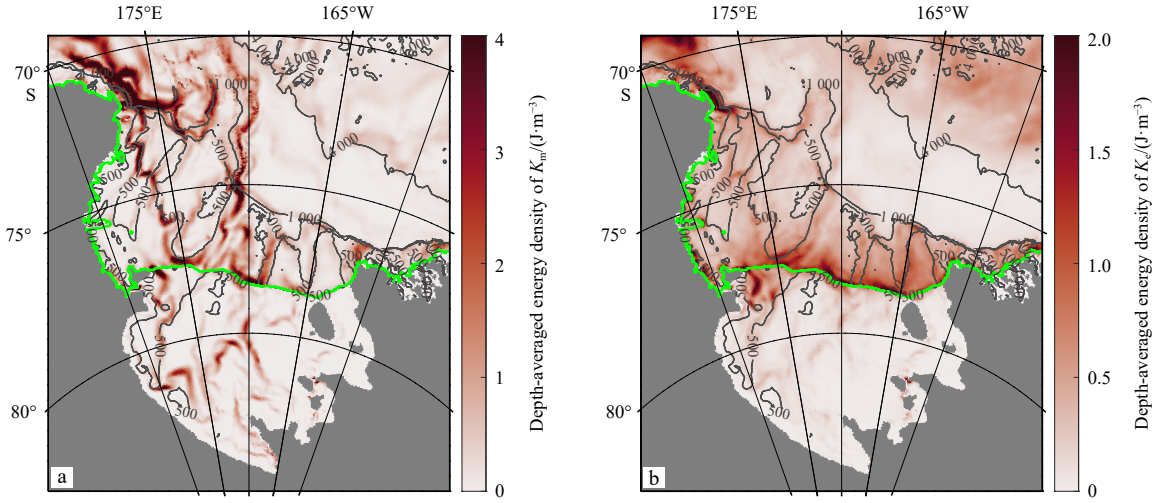


Fig. 2. Distributions of the depth-averaged energy density of K_m (a) and K_e (b). The solid green lines represent the coastline and the ice shelf calving front. The thin grey lines represent the 500 m, 1 000 m, and 4 000 m isobaths.

is induced by the basal melting of the ice shelves.

A zonal band of large K_e is identified along the RIS front and spread out offshore away from the coastline (Fig. 2b), and large K_e is also identified over the northwestern continental slope. Large values of K_e extend into the northwestern flank of the RIS cavity where warm surface water can flow into the RIS cavity (Malyarenko et al., 2019), but such strong K_e do not extend much farther into the RIS cavity, implying the suppressing effects of the ice cavity on the time-varying circulations. Overall, the spatial distributions of K_m and K_e in the Ross Sea region are very different, yet K_m and K_e are both strong over the northwestern continental slope.

In order to assess the vertical structure of KE, Fig. 3 shows the area-averaged K_m and K_e. From the sea surface to the seafloor, the volume-integrated K_m is found to be about 1.04 PJ (1 PJ = 10^{15} J), while the total K_e amounts to about 0.82 PJ. In the sea surface layer, K_e (about 2.11 J/m^3) is much larger than K_m (about 0.91 J/m^3). Both K_m and K_e decrease rapidly with increasing depth within the 1 000 m upper layer, yet the decreasing of K_e is stronger than K_m. At the 1 000 m depth, K_e (about 0.17 J/m^3) is already weaker than K_m (about 0.30 J/m^3). Beneath the 1 000 m depth, both K_m and K_e show a much slower decreasing rate. So, K_m and K_e have a general similarity in the deep layer. Therefore, it is interesting to know the differences of the KE distribution between the water column in the upper 1 000 m and below the 1 000 m depth. Volume-integrated K_m and K_e from the sea surface to 1 000 m are about 0.53 PJ and 0.57 PJ, while volume-integrated K_m and K_e from 1 000 m depth to the sea floor are about 0.51 PJ and 0.25 PJ, respectively. The energy of the K_m in the upper 1 000 m is almost the same as that below the 1 000 m depth. Yet, the integrated K_e in the upper 1 000 m layer is almost twice as the energy in the deeper depths.

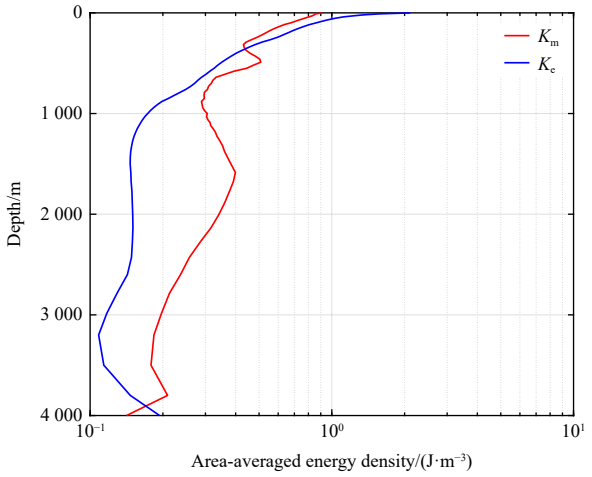


Fig. 3. Vertical profiles of the area-averaged energy densities of K_m (red) and K_e (blue) over the Ross Sea.

For the APE of time-averaged and time-varying circulations, P_m and P_e, are shown as the depth-averaged values in Fig. 4. The spatial pattern of P_m shows that the APE of time-averaged circulations in the western Ross Sea is much higher than in the eastern Ross Sea (Fig. 4a). Over the continental shelf, the maximal P_m is identified in the southwestern region where intensive brine rejection occurs in the polynya in winter due to the production of sea ice (Tamura and Ohshima, 2011; Tamura et al., 2011). Beneath the RIS, P_m in the western and middle cavity are also much stronger than in the southeastern flank, implying that the relatively larger P_m in the sub-ice-shelf cavity may be closely associated with the intrusion of Dense Shelf Water (Holland et al., 2003; Mack et al., 2019; Yan et al., 2023), which is produced by the brine rejection.

The spatial distribution of P_e is similar to K_e, with larger values identified along the RIS front and in the northwestern continental slope (Fig. 4b), implying that the spatial distribution of K_e may be dominated by P_e rather than K_m. The similarities between the horizontal structure of P_e and K_e have also been usually found in global oceans (Roullet et al., 2014; Wu et al., 2017). It is also ev-

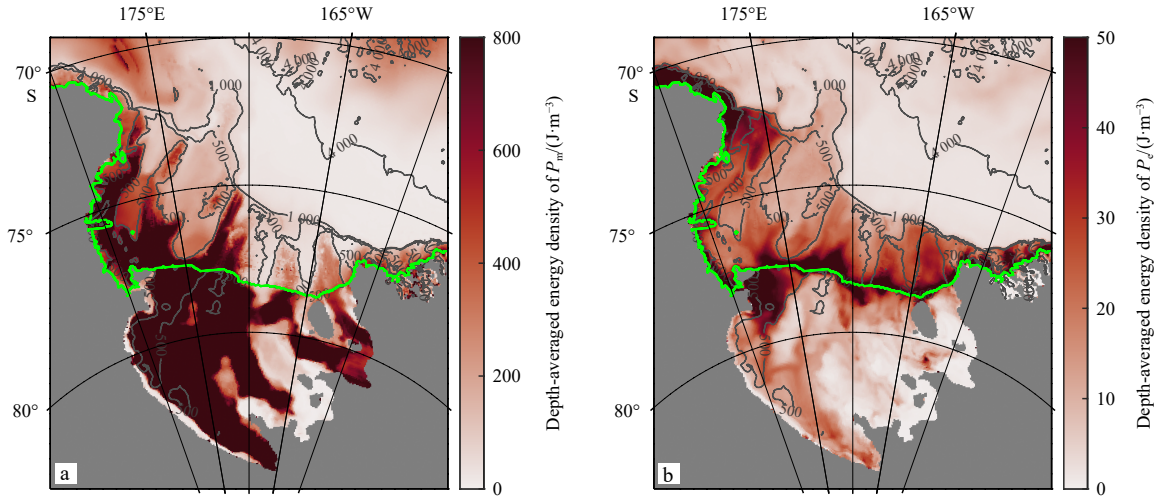


Fig. 4. Distributions of the depth-averaged energy densities of P_m (a) and P_e (b). The solid green lines represent the coastline and the ice shelf calving front.

ident that the APE associated with time-varying circulations is considerably lower north of the 1 000 m isobaths, akin to the distribution of P_m. Beneath the RIS, the maximal P_e is found in the northwestern flank where strong K_e extends into the RIS cavity (Fig. 2b), suggesting that P_e may still be intimately related to K_e in the sub-ice-shelf cavity.

In order to assess the vertical structure of APE, the area-averaged energy densities of P_m and P_e are shown in Fig. 5. In contrast to the vertical structure of KE, Fig. 5 illustrates that the APE of time-mean and time-varying circulations are mostly concentrated in the upper layer, coinciding with the lower values of APE to the north of 1 000 m isobaths shown in Fig. 4. It is also evident that P_m peaks at both the sea surface and about 550 m depth, whereas P_e predominantly concentrates at the sea surface. On average, P_m is larger than P_e throughout the water column.

From the sea surface to the seafloor, the volume-integrated P_m is up to about 527.62 PJ, while the total P_e only amounts to about 19.20 PJ. Different from KE of the time-mean and time-varying circulations, P_m (about 381.76 J/m^3) is much larger than P_e (about 248.80 J/m^3) at the surface layer. Both P_m and P_e decrease drastically to about 88.58 J/m^3 and 25.45 J/m^3 at the 30 m depth, respectively. Yet, P_m increases towards the deeper depth and reaches the second maximum at 550 m depth, with an extreme of about 2 465.88 J/m^3. Compared to the KE of time-mean and time-varying circulations, P_m gradually decreases to about 0 J/m^3 at about 3 000 m depth, and P_e almost vanishes at 1 000 m depth. Volume-integrated P_m from the sea surface to 3 000 m depth is about 524.95 PJ, and volume-integrated P_e from the sea surface to 1 000 m depth is about 17.95 PJ.

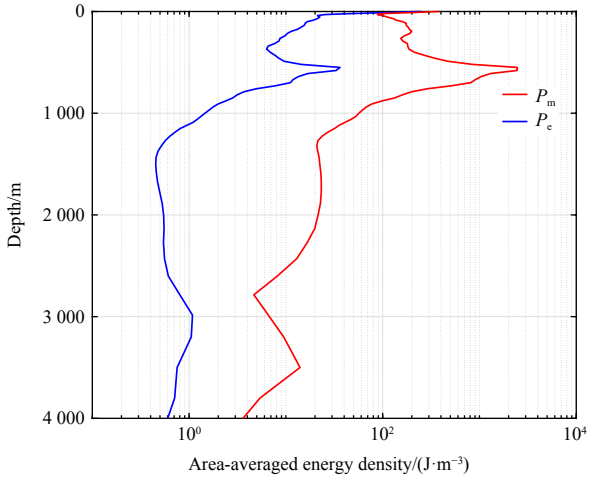


Fig. 5. Vertical profiles of the area-averaged energy densities of P_m (red) and P_e (blue) over the Ross Sea.

5 Generation of KE and APE

In this section, according to Eqs (9)−(12), we calculated the terms of energy reservoirs $G(K_m)$, $G(K_e)$, $G(P_m)$, and $G(P_e)$.

Figure 6 illustrates the spatial distributions of the KE provided by the wind stress. The time-mean wind stress supplies the power of $G(K_m)$ to the time-mean circulations, with an area-integrated value of about 0.36 GW (1 GW = 10^9 W). The power supplied by the time-varying winds to the time-varying circulations, $G(K_e)$, is up to about 2.84 GW.

Alternative positive and negative values of $G(K_m)$ are shown over the continental shelf (Fig. 6a), implying that the circulation structure is steered by the complex topographic features rather than the local wind. It is worth noting that positive values are often identified over the eastern flanks of submarine troughs, while negative values generally occupy the western flanks of submarine troughs. Such a spatial pattern is consistent with the local offshore winds and the onshore currents along the eastern flank and

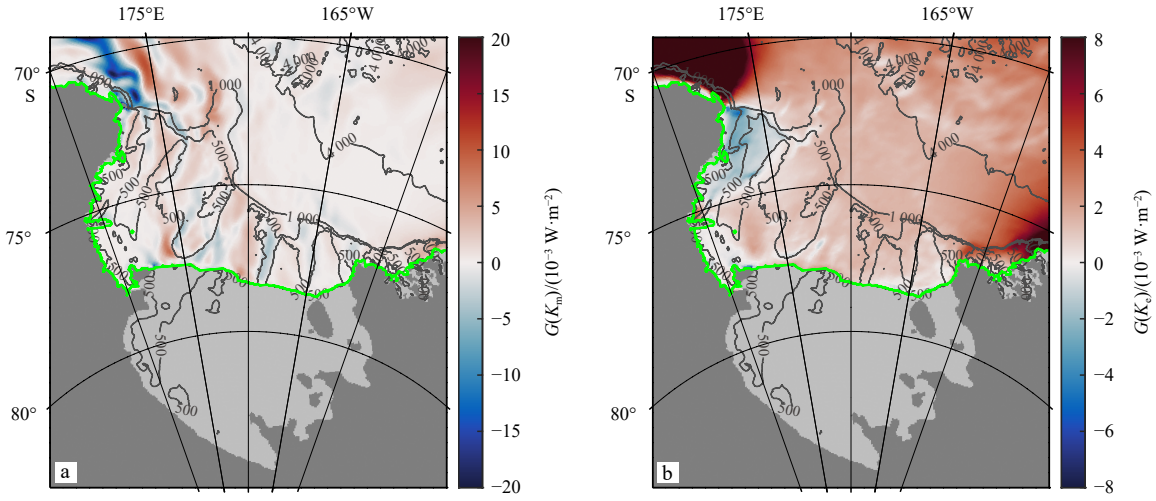


Fig. 6. Horizontal distributions of the power input to the time-mean circulations by time-mean wind stress $G(K_m)$ (a) and the power input to the time-varying circulations by the time-varying wind stress $G(K_e)$ (b). The solid green lines represent the coastline and the ice shelf calving front.

offshore currents along the western flank of submarine troughs. $G(K_m)$ has relatively large negative values north of 1 000 m isobath and west of 173°E. The wind stress is generally northward over the northwestern Ross Sea, yet there is a current loop existing north of 1 000 m isobath and west of 175°E. Thus, $G(K_m)$ shows a strong zonal gradient over the northwestern Ross Sea. Therefore, the strong K_m shown over the northwestern region (Fig. 2a) should not be attributed to the power input of the local wind stress $G(K_m)$ (Fig. 6a).

Since $G(K_e)$ generally shows positive values in the Ross Sea, with the exception of the northwestern continental shelf region (Fig. 6b). Generally, the direction of time-varying circulations should be dominated by the orientation of time-varying winds (Zhang et al., 2023), with the maximal $G(K_e)$ of more than 8×10^{-3} W/m^2 occurring over the northwestern deep ocean. In contrast, with the minimal $G(K_e)$ of less than -2×10^{-3} W/m^2 occurring over the western continental shelf region, and $G(K_e)$ is relatively weak along the RIS front and even shows small negative values close to McMurdo Sound (MMS). The differences of the spatial distributions between K_e and $G(K_e)$ suggest that K_e along the RIS front originates not only from the external time-varying wind stress but also internal oceanic processes (Fig. 2b). Wang and Huang (2004) proposed that most wind energy input into general oceanic flows dissipates within the Ekman layer, and thereby $G(K_e)$ is not expected to be able to drive deep-ocean currents and internal mixing. So, K_e is largely confined within the surface layer (Fig. 3).

Figure 7 shows the spatial distributions of the APE provided by the buoyancy flux at the sea surface and the ocean-ice shelf interface. At the sea surface, the time-mean and time-varying buoyancy flux supplies the power of $G(P_m)$ and $G(P_e)$ to the time-mean and time-varying circulations, with an area-integrated value of about 1.47 GW and 2.11 GW, respectively. In the sub-ice-shelf cavity, the area-integrated power by $G(P_m)$ tends to provide APE to the ocean, amounting to about 24.65 MW (1 MW = 10^6 W). $G(P_e)$ also provides APE into the ocean, amounting to about 183.77 MW.

$G(P_m)$ is almost positive on the continental shelf, with remarkable large values along the RIS front, in the MMS, and the TNB (Fig. 7a). Such a strong contribution of $G(P_m)$ near the coastal region is expected to be correlated with the Ross Sea Polynya and the Terra Nova Bay Polynya where brine rejection and heat loss occur in winter (see Figs S2−S5, S10−S17, S22−S23, and S25). The

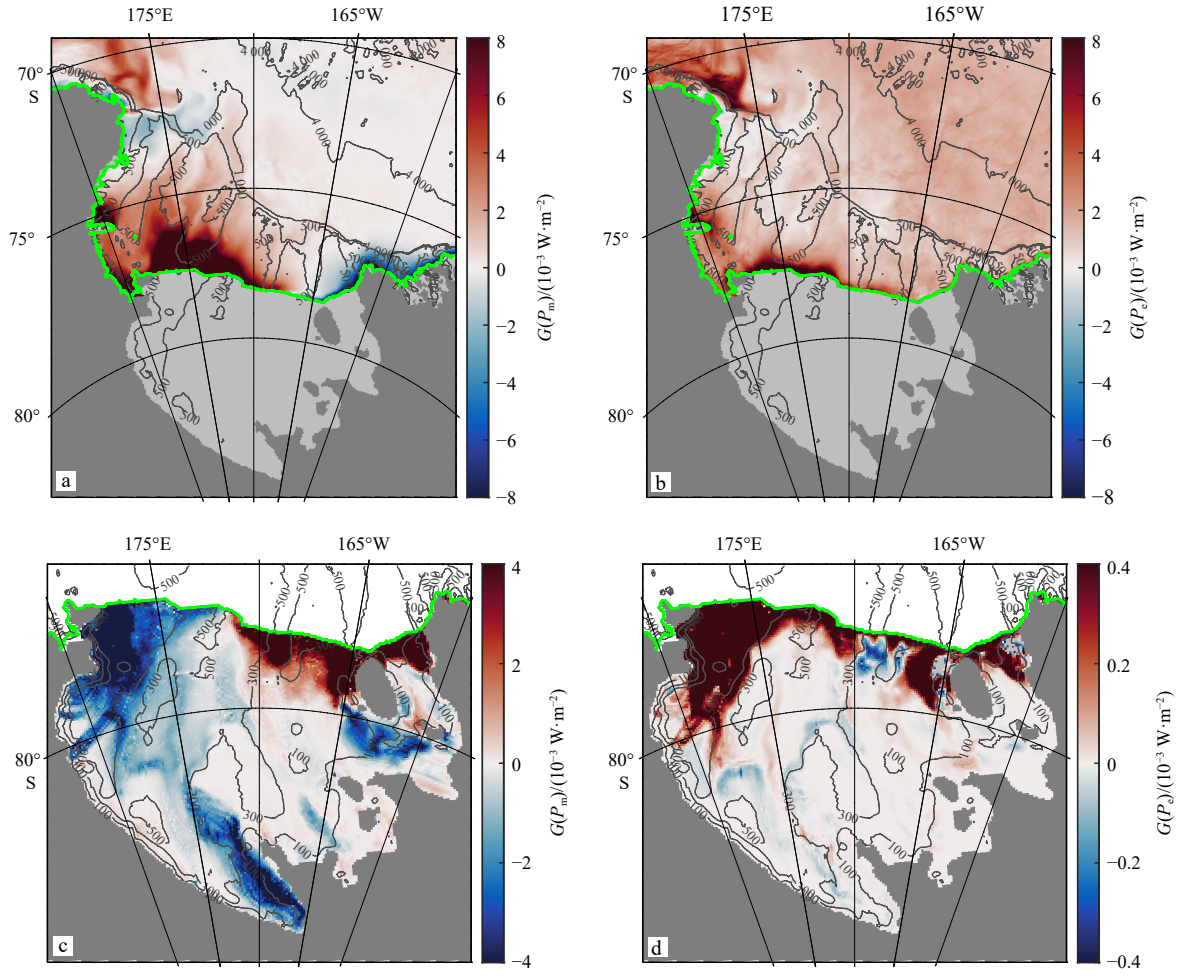


Fig. 7. Distributions of $G(P_m)$ (a and c) and $G(P_e)$ (b and d): a and b. in the open ocean; c and d. in the sub-ice-shelf cavity. The solid green lines represent the coastline and the ice shelf calving front.

area-integrated contribution of freshwater flux to $G(P_m)$ is about 1.46 GW, and that is much larger than the area-integrated contribution from heat flux of about 0.01 GW, implying the effects of the sea ice on the ocean by isolating the impacts of cold air in winter. $G(P_m)$ is determined by the surface buoyance and the density variance. In the Ross Sea, the positive area-integrated $G(P_m)$ indicates that the generation of density difference is in excess of the removal of density difference, and the contribution of the freshwater flux (brine rejection) is much more efficient than the heat flux.

In contrast, the major differences between $G(P_e)$ and $G(P_m)$ are that $G(P_e)$ has values larger than 2×10^{-3} W/m^2 over a broad region, with maximum values along the RIS front and in the TNB (Fig. 7b). Yet, $G(P_e)$ does not have strong power input in the MMS as $G(P_m)$, and the spatial extension of lager $G(P_e)$ along the RIS front is also smaller than $G(P_m)$. The area-integrated contribution of freshwater flux to $G(P_e)$ is about 2.10 GW, and that is also larger than the area-integrated contribution from heat flux of about 0.01 GW, implying that the influences of brine rejection are stronger than heat loss. So, the freshwater flux plays a dominant role in the generation of both P_m and P_e in the Ross Sea.

In the sub-ice-shelf cavity, the circulations are mainly driven by the buoyancy, i.e., the "ice pump" (Lewis, 1985). In the RIS cavity, the basal melting of the RIS is predominant (Rignot et al., 2013; Yan et al., 2023) (see Figs S32 and S34), and thereby a negative value is expected to dominate the spatial pattern of $G(P_m)$ at the ocean-ice shelf interface (Fig. 7c). The minimal $G(P_m)$ occurs in the northwestern flank of the RIS cavity, with a negative band extending to the deep southern grounding line. Yet, positive value is also identified over the northeastern flank of the RIS, and such positive $G(P_m)$ should be attributed to the local negative ρ^* (see Fig. S36).

Compared to $G(P_m)$, $G(P_e)$ is much smaller in the sub-ice-shelf cavity (Fig. 7d), with a maximum shown in the northwestern flank and along the western and middle RIS front (note the differences of color bars). The position of the maximum of $G(P_e)$ is largely inconsistent with the minimum of $G(P_m)$ (Fig. 7c), and the northwestern flank of the RIS cavity is the key region where the surface warm water can intrude into the sub-ice-shelf cavity by the wedge mechanism (Malyarenko et al., 2019) (Fig. 7d). Overall, the freshwater flux component of $G(P_m)$ beneath the RIS provides the energy to P_m by the area-integrated power of about 24.64 MW, and the freshwater flux component of $G(P_e)$ provides the energy to P_e by the area-integrated power of about 183.76 MW. Analogous to the contribution over the continental shelf, the freshwater flux still plays a dominant role in both $G(P_m)$ and $G(P_e)$ in the RIS cavity.

6 Conversions between the four energy reservoirs

In this section, according to Eqs (13)–(16), we calculated the terms of energy reservoirs $C(P_m,P_e)$, $C(P_e,K_e)$, $C(P_m,K_m)$ and, $C(K_e,K_m)$.

Figure 8 presents the vertical integrations of $C(P_m,P_e)$ and $C(P_e,K_e)$ that represent the conversion in the baroclinic production. When the direction of the eddy density flux $(\rho' \boldsymbol{u}_h')$ is parallel with the mean density gradient, energy conversion occurs between P_m and P_e. $C(P_m,P_e)$ in the Ross Sea region mostly occurs along the RIS front and north of the 4 000 m isobaths (Fig. 8a), with large positive values implying that the conversion is predominantly from P_m to P_e. Along the RIS front, the coastal current is generally westward, and the zonal gradient of ρ^* $(\partial\rho^*/\partial x)$ is often negative (see Fig. S35). Since positive $C(P_m,P_e)$ indicates that the energy is converted from P_m to P_e, based on Eq. (16), the $\overline{\rho' u'}$ is expected to be the down-gradient zonal eddy density flux along the RIS front, with positive values along the RIS front.

Figure 8b illustrates the vertical integration of

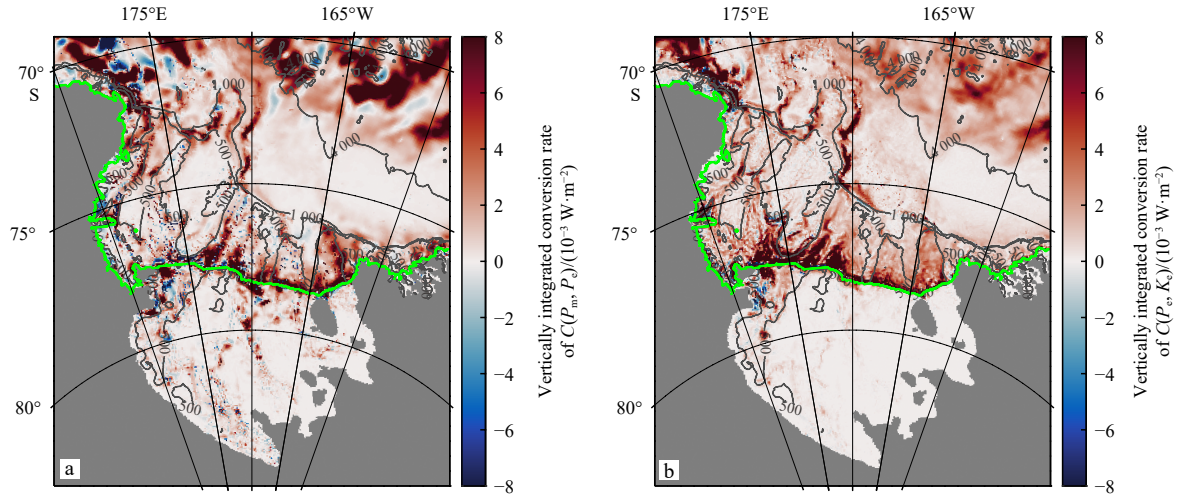


Fig. 8. Vertically integrated conversion rate of $C(P_m,P_e)$ (a) and $C(P_e,K_e)$ (b). The solid green lines represent the coastline and the ice shelf calving front.

$C(P_e,K_e)$. According to Eq. (14), the conversion between P_e and K_e depends on the covariance between ρ' and w'. Downward movement of positive ρ' (denser water masses) and upward movement of negative ρ' (lighter water masses) result in the positive value of $C(P_e, K_e)$, and vice versa. $C(P_e,K_e)$ represents the conversion from P_e to K_e in the baroclinic pathway, and the spatial distribution of $C(P_e,K_e)$ indicates that baroclinicity prevails along the RIS front and spread northward within the submarine troughs. There is a good consistency between K_e and $C(P_e,K_e)$ near the coastal region, as indicated by large K_e along the RIS front (Fig. 2b). The strong K_e is also related to baroclinicity over the northwestern slope where $C(P_e,K_e)$ is positive.

Beneath the RIS, both $C(P_m,P_e)$ and $C(P_e,K_e)$ are relatively weak. Yet, $C(P_m,P_e)$ still can occur in the south of the RIS front, while $C(P_e,K_e)$ is generally confined to the north of the RIS front, except in the northwestern flank of the RIS cavity. By the baroclinic production, the total volume-integrated conversion is directed from P_m to P_e and amounts to about 2.82 GW, and the volume-integrated $C(P_m,P_e)$ in the RIS cavity is about 269.81 MW. The total volume-integrated conversion from P_e to K_e amounts to about 2.86 GW, and the volume-integrated $C(P_e,K_e)$ in the RIS cavity is about 162.18 MW.

Figure 9 shows the vertical integrations of $C(P_m,K_m)$ and $C(K_e,K_m)$ that represent the conversions in the barotropic production. When relatively light (dense) water masses are moved upwards (downwards), energy conversion occurs from P_m to K_m, and vice versa. $C(K_e,K_m)$ can be decomposed into two terms. The first term, $\overline{u'\boldsymbol{u}'}\cdot\nabla\bar{u}$, is related to the horizontal gradient of $\bar{u}$, and the second term, $\overline{v'\boldsymbol{u}'}\cdot\nabla\bar{v}$, is related to the horizontal gradient of $\bar{v}$.

Along the continental slope, large values of $C(P_m,K_m)$ change their sign within a short distance (Fig. 9a). Since ρ^* does not change its sign within such a small scale (see Fig. S35), the alternatively positive and negative values of $C(P_m,K_m)$ should be attributed to the abrupt sign change in the vertical velocity. Over the continental slope, vertical transport is usually associated with cross-slope exchanges of water masses, implying that cross-slope overflows and intrusions may occur intensively. There are also large positive and negative values in the TNB polynya and along the western RIS front polynya. The deep convection in polynyas brings Dense Shelf Water downward, while the buoyant Ice Shelf Water upwells and flows out from the ice shelf front. Therefore, the complex vertical velocity field along the front of ice shelves may be responsible for the intensive conversion between P_m to K_m. In the RIS cavity, active $C(P_m,K_m)$ is concentrated on the western and middle flank (Fig. 9a), consistent with the spatial pattern of K_m in the RIS cavity (Fig. 2a). In the sub-ice-shelf cavity, as the atmospheric forcing vanishes, the KE of the oceanic circulations are mainly determined by $C(P_m,K_m)$ and $C(K_e,K_m)$. The similarity of $C(P_m,K_m)$ and K_m implies that $C(P_m,K_m)$ should play a dominant role in driving KE in the RIS cavity.

Similarly, $C(K_e,K_m)$ is also dominated by small scale structures of positive and negative values (Fig. 9b), yet the magnitude of $C(K_e,K_m)$ is much smaller than $C(P_m,K_m)$. Large values of $C(K_e,K_m)$ are located mainly along the RIS front and over the northwestern slope where K_e is also relatively large. In the two terms of $C(K_e,K_m)$, the positive $\overline{u'u'}\cdot\nabla\bar{u}$ (about 0.03 GW), makes a larger contribution than the negative $\overline{v'u'}\cdot\nabla\bar{v}$ (about −0.01 GW), indicating the dominant role of shear instability related to the mean zonal flows. In the RIS cavity, active $C(K_e,K_m)$ is concentrated on the northwestern flank, consistent with the spatial pattern of K_e in the RIS cavity (Fig. 2b). The similarity of the spatial distributions between $C(K_e,K_m)$ and K_e implies that K_m may also convert energy from the time-mean circulations to the time-varying circulations in the RIS cavity.

In previous studies that focused on the global ocean and the Southern Ocean, KE are generally converted from

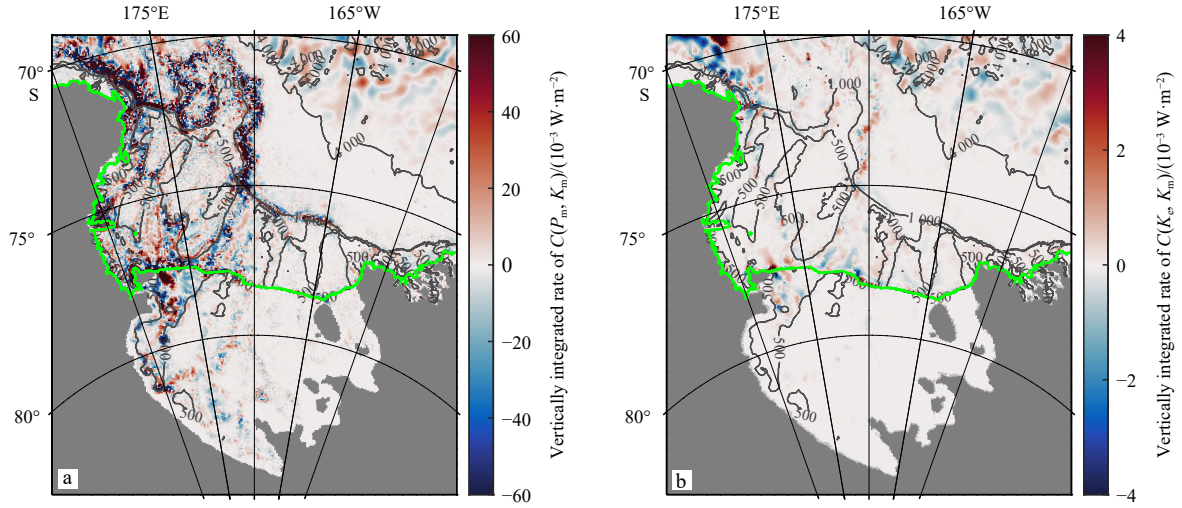


Fig. 9. Vertically integrated rates of $C(P_m,K_m)$ (a) and $C(K_e,K_m)$ (b). The solid green lines represent the coastline and the ice shelf calving front.

K_m to K_e (von Storch et al., 2012; Chen et al., 2014; Wu et al., 2017). However, in the Ross Sea, K_e changes from a KE sink to a KE source, transferring power to K_m through the barotropic pathway. Such an inverse energy cascade pathway has also been identified in the Weddell Sea (Jüling et al., 2018). By the barotropic production, the total volume-integrated conversion is directed from P_m to K_m and amounts to about 4.57 GW, and the volume-integrated $C(P_m,K_m)$ in the RIS cavity is about 265.75 MW. The total volume-integrated conversion from K_e to K_m amounts to about 0.02 GW, and the volume-integrated from $C(K_e,K_m)$ in the RIS cavity is about −4.88 MW.

7 LEC in the Ross Sea and in the RIS cavity

Considering the different surface forcing between the open ocean and the RIS cavity, the LEC are analyzed within the open ocean and the RIS cavity, respectively.

The LEC for the Ross Sea is shown in Fig. 10. Similar to previous studies (von Storch et al., 2012; Wu et al., 2017; Jüling et al., 2018; Ssebandeke et al., 2024), since P_m depends on the choice of reference density, the energy in P_m is much larger than the other three energy reservoirs. Disregarding P_m (527.62 PJ), P_e is the largest and amounts to about 19.20 PJ, followed by K_m of about 1.04 PJ and K_e of about 0.82 PJ.

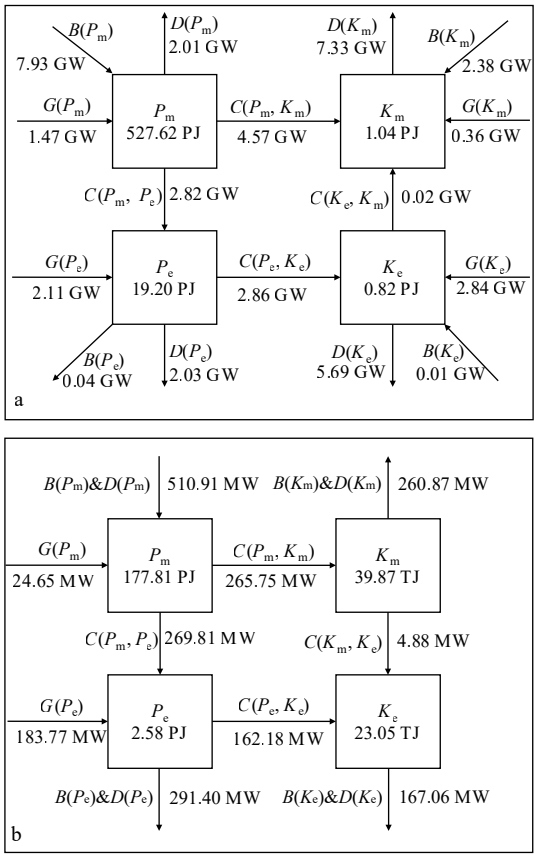


Fig. 10. LEC for the Ross Sea (a) and LEC for the RIS cavity (b). Energy reservoirs are in units of PJ, and rates of generation, conversion, dissipation, and boundary fluxes are either in units of GW. Energy reservoirs are in units of PJ or TJ (1 TJ = 10^{12} J), and rates of energy input and transfer are in units of MW. Arrows indicate the energy transfer directions.

Regarding the conversion rate in the Ross Sea (Fig. 10a), the energy cascade is mainly through the baroclinic pathway $P_m \rightarrow P_e \rightarrow K_e$. The conversion from P_e to K_e is almost two times larger than the conversion from P_m to P_e. As a result, both P_m and $G(P_e)$ are important power suppliers to P_e, and then the time-varying circulations are generated by the baroclinic pathway $P_e \rightarrow K_e$. In the barotropic pathway, the conversion between P_m and K_m is much stronger than that between K_m and K_e. Fueled by the buoyancy flux, P_m converts its APE into the KE of K_m by vertical transport, and strong vertical velocity mostly occurs along the continental slope and the RIS front. In addition, easterlies around the Antarctic marginal seas tend to be associated with downward Ekman pumping, and the consequent mean vertical velocity can also result in the positive value of area-mean $C(P_m,K_m)$. In the Ross Sea, $C(K_e,K_m)$ is weak and directed toward K_m, and such an inverse energy cascade is different from that in the broad Southern Ocean (Wu et al., 2017; Jüling et al., 2018). K_m is mainly supplied by $G(K_m)$ and $C(P_m,K_m)$, and $G(P_m)$ is the only energy source of P_m. Therefore, the time-mean circulations in the Ross Sea are determined by the surface momentum forcing directly and the buoyance forcing indirectly. Overall, the time-mean circulations are mainly generated by the barotropic pathway $P_m \rightarrow K_m \leftarrow K_e$.

In the Ross Sea, the power input is mainly supplied by the buoyancy forcing (Fig. 10a). The total power input is about 6.78 GW, with the buoyancy forcing of about 3.58 GW and the wind forcing of about 3.20 GW, respectively. More than half of the KE of the oceanic circulations needs to invoke the buoyancy forcing rather than being forced by the winds only. Such strong power supplied by $G(P_m)$ and $G(P_e)$ around the Antarctic marginal seas is substantially different from that in the broad Southern Ocean (Wu et al., 2017; Jüling et al., 2018). The energy flows at the open boundaries of the selected region are much weaker than the conversion rate in the interior region. Regarding energy reservoirs in the interested region, the rates of production and dissipation are relatively larger than the rate of conversion (Fig. 10a), implying that the energy generation and boundary fluxes essentially balance the energy dissipation.

In contrast to the oceanic circulations driven by the atmospheric forcing, the circulations in the RIS cavity are much weak. Regarding the energy reservoirs in the RIS cavity (Fig. 10b), P_m is the largest in the RIS cavity (177.81 PJ), followed by P_e of about 2.58 PJ, K_m of about 39.87 TJ, and K_e of about 23.05 TJ.

Regarding the conversion rate in the RIS cavity (Fig. 10b), the energy cascade is also dominated by the baroclinic pathway $P_m \rightarrow P_e \rightarrow K_e$. $C(P_m,P_e)$ amounts to about 269.81 MW, and then the APE of P_e is converted to

KE of K_e by the power of about 162.18 MW. In the barotropic pathway, $C(P_m,K_m)$ of about 265.75 MW is much stronger than $C(K_e,K_m)$ of about −4.88 MW. In the absence of atmospheric forcing in the RIS cavity, P_m is the only dominant energy supplier of K_m. In contrast to $C(K_e,K_m)$ in the selected region (Fig. 10a), KE is weakly directed from K_m toward K_e in the RIS cavity. Thus, the time-varying circulations in the RIS cavity can also be fueled by the barotropic pathway $P_m \rightarrow K_m \rightarrow K_e$. In the RIS cavity, the power input is only supplied by the buoyancy forcing (Fig. 10b). $G(P_m)$ supplies power of about 24.65 MW to P_m, and $G(P_e)$ supplies power of about 183.77 MW to P_e.

8 Summary and discussion

A coupled regional ocean-sea ice-shelf model is used to study the LEC in the Ross Sea and the RIS cavity. Based on the simulated results of this eddy-permitting model, we focused on the characteristics of the energy reservoirs, energy generations, and energy conversions.

K_m is highly inhomogeneously distributed and amounts to a total of about 1.04 PJ, with energetic currents concentrated along the RIS front, submarine troughs, and the continental slope. The total K_m in the RIS cavity is about 39.87 TJ, and K_m in the western and middle flanks of the RIS cavity is relatively larger than in the eastern flank. The spatial pattern of K_e is smoothly spread out from the RIS front and amounts to a total of about 0.82 PJ. The total K_e in the RIS cavity is about 23.05 TJ, with large values extending into the northwestern flank. P_m is concentrated in the southwestern continental shelf, with a total of about 527.62 PJ. In the RIS cavity, P_m is relatively large in the western flank and amounts to about 177.81 PJ. Strong P_e occurs along the RIS front and the northwestern slope, with a total of about 19.20 PJ. Beneath the RIS, P_e is confined around the RIS front and only amounts to about 2.58 PJ.

In the Ross Sea, the power is transferred away from P_m, mainly via the pathway $K_m \leftarrow P_m \rightarrow P_e \rightarrow K_e$. The baroclinic pathway is the main path to convert P_e to K_e in the ocean, and the total rate amounts to about 2.86 GW. In the RIS cavity, the energy conversion pathway is the same as in the Ross Sea, with the conversion from P_e to K_e reaching about 162.18 MW. In contrast, the energy conversion in the barotropic pathway in the Ross Sea is opposite to that in the Southern Ocean (Wu et al., 2017; Jüling et al., 2018). K_m tends to source energy from P_m and K_e via the barotropic pathway $P_m \rightarrow K_m \leftarrow K_e$, with the inverse energy cascade from K_e to K_m of about 0.02 GW. Beneath the RIS, the KE is directed from K_m to K_e, with a relatively weak rate of about 4.88 MW. Such a barotropic pathway from the time-mean circulations to the time-varying circulations is similar to that in the Amery Ice Shelf cavity (Wu et al., 2021).

The total power input to the ocean is about 6.78 GW, of which about 3.58 GW comes from the buoyancy forcing and 3.20 GW from the winds. The total dissipation of K_m and K_e amounts to about 13.02 GW, and $D(K_e)$ is about three times more than $D(K_m)$. In the RIS cavity, without the atmospheric forcing, only the buoyance forcing contributes to about 208.42 MW.

This study still has some limitations. First, the uncertainties in the topography and geometry of the sub-ice-shelf cavity may result in uncertainties in our simulation. The basal melting rate of ice shelves is closely related to the depth of the ice draft, yet the uncertainties of the grounding lines are still relatively large due to limited observations (Fretwell et al., 2013). Second, the horizontal resolution of this coupled model is still not fine enough to fully resolve mesoscale eddies in the Ross Sea (Mack et al., 2019). Based on the simulated results from this eddy-permitting model, our analysis may still underestimate K_e and corresponding conversion terms. Third, the vertical resolution of this coupled model is relatively coarse in the deep layers. Since a finer vertical resolution can remarkably decrease the overestimation of the simulated basal melting of ice shelves (Schodlok et al., 2016), the increase in the vertical resolution may improve the LEC analysis in the RIS cavity. Fourth, this coupled model has not introduced the simulation of frazil ice. Frazil ice has been found to be important in regulating the basal melting/freezing rate of ice shelves (Galton-Fenzi et al., 2012; Cheng et al., 2019). The lack of the simulation of frazil ice may influence the simulated basal melting/freezing and the characteristics of Ice Shelf Water.

Future studies focused on the LEC in the Ross Sea would benefit from an increase in both horizontal and vertical resolution of a regional coupled model. The inclusion of a frazil ice model could improve the simulation in the sub-ice-shelf cavity. By using the eddy-resolving models in future studies, the assessments of the properties and three-dimensional characteristics of mesoscale eddies may also provide insights into the influences of the time-varying circulations.

Acknowledgement

The authors are grateful to the great support from the High-performance Computing Platform of Hohai University to this work.

References

Arndt J E, Schenke H W, Jakobsson M, et al. 2013. The International Bathymetric Chart of the Southern Ocean (IBCSO) version 1.0—A new bathymetric compilation covering circum-Antarctic waters. Geophysical Research Letters, 40(12): 3111–3117, doi: 10.1002/grl.50413

Biddle L C, Swart S. 2020. The observed seasonal cycle of submesoscale processes in the Antarctic marginal ice zone. Journal of Geophysical Research: Oceans, 125(6): e2019JC015587, doi: 10.1029/2019JC015587

Castagno P, Capozzi V, DiTullio G R, et al. 2019. Rebound of

shelf water salinity in the Ross Sea. Nature Communications, 10(1): 5441, doi: 10.1038/s41467-019-13083-8

Castagno P, Falco P, Dinniman M S, et al. 2017. Temporal variability of the Circumpolar Deep Water inflow onto the Ross Sea continental shelf. Journal of Marine Systems, 166: 37–49, doi: 10.1016/j.jmarsys.2016.05.006

Chelton D B, deSzoeke R A, Schlax M G, et al. 1998. Geographical variability of the first baroclinic rossby radius of deformation. Journal of Physical Oceanography, 28(3): 433–460, doi: 10.1175/1520-0485(1998)028<0433:GVOTFB>2.0.CO;2

Chen Ru, Flierl G R, Wunsch C. 2014. A description of local and nonlocal eddy-mean flow interaction in a global eddy-permitting state estimate. Journal of Physical Oceanography, 44(9): 2336–2352, doi: 10.1175/JPO-D-14-0009.1

Cheng Chen, Jenkins A, Holland P R, et al. 2019. Responses of sub-ice platelet layer thickening rate and frazil-ice concentration to variations in ice-shelf water supercooling in McMurdo Sound, Antarctica. The Cryosphere, 13(1): 265–280, doi: 10.5194/tc-13-265-2019

Cox M D. 1985. An eddy resolving numerical model of the ventilated thermocline. Journal of Physical Oceanography, 15(10): 1312–1324, doi: 10.1175/1520-0485(1985)015<1312:AERNMO>2.0.CO;2

Ferrari R, Wunsch C. 2009. Ocean circulation kinetic energy: Reservoirs, sources, and sinks. Annual Review of Fluid Mechanics, 41: 253–282, doi: 10.1146/annurev.fluid.40.111406.102139

Ferrari R, Wunsch C. 2010. The distribution of eddy kinetic and potential energies in the global ocean. Tellus A, 62(2): 92–108, doi: 10.1111/j.1600-0870.2009.00432.x

Fetterer F, Knowles K, Meier W N, et al. 2017. Sea Ice Index, Version 3 [Data Set]. Boulder, CO, USA: National Snow and Ice Data Center, doi: 10.7265/N5K072F8

Fretwell P, Pritchard H D, Vaughan D G, et al. 2013. Bedmap2: improved ice bed, surface and thickness datasets for Antarctica. The Cryosphere, 7(1): 375–393, doi: 10.5194/tc-7-375-2013

Galton-Fenzi B K, Hunter J R, Coleman R, et al. 2012. Modeling the basal melting and marine ice accretion of the Amery Ice Shelf. Journal of Geophysical Research: Oceans, 117(C9): C09031, doi: 10.1029/2012JC008214

Herraiz-Borreguero L, Allison I, Craven M, et al. 2013. Ice shelf/ocean interactions under the Amery Ice Shelf: Seasonal variability and its effect on marine ice formation. Journal of Geophysical Research: Oceans, 118(12): 7117–7131, doi: 10.1002/2013JC009158

Hersbach H, Bell B, Berrisford P, et al. 2020. The ERA5 global reanalysis. Quarterly Journal of the Royal Meteorological Society, 146(730): 1999–2049, doi: 10.1002/qj.3803

Holland D M, Jacobs S S, Jenkins A. 2003. Modelling the ocean circulation beneath the Ross Ice Shelf. Antarctic Science, 15(1): 13–23, doi: 10.1017/s0954102003001019

Huang Ruixin. 2004. Ocean, energy flows in. In: Cleveland C J, ed. Encyclopedia of Energy. Amsterdam: Elsevier, 497–509, doi: 10.1016/B0-12-176480-X/00053-X

Huang Ruixin. 2005. Available potential energy in the world's oceans. Journal of Marine Research, 63(1): 141–158, doi: 10.1357/0022240053693770

Jüling A, Viebahn J P, Drijfhout S S, et al. 2018. Energetics of the southern ocean mode. Journal of Geophysical Research: Oceans, 123(12): 9283–9304, doi: 10.1029/2018JC014191

Kang Dujuan, Curchitser E N. 2015. Energetics of eddy-mean flow interactions in the Gulf Stream region. Journal of Physical Oceanography, 45(4): 1103–1120, doi: 10.1175/JPO-D-14-0200.1

Lewis E L. 1985. The "Ice Pump", a Mechanism for Ice-shelf Melting, in Glaciers, Ice Sheets, and Sea Level: Effect of a CO_2-induced Climate Change. Rep. DOE/EV/60235–1. Washington: U. S. Dep. of Energy, 275–278

Locarnini R A, Mishonov A V, Baranova O K, et al. 2019. World ocean atlas 2018, volume 1: temperature. A. Mishonov, ed. NOAA Atlas NESDIS, 81: 52, https://archimer.ifremer.fr/doc/00651/76338/77329.pdf [2019-07-01]

Lorenz E N. 1955. Available potential energy and the maintenance of the general circulation. Tellus, 7(2): 157–167, doi: 10.3402/tellusa.v7i2.8796

Losch M, Menemenlis D, Campin J M, et al. 2010. On the formulation of sea-ice models. Part 1: Effects of different solver implementations and parameterizations. Ocean Modelling, 33(1−2): 129–144, doi: 10.1016/j.ocemod.2009.12.008

Mack S L, Dinniman M S, Klinck J M, et al. 2019. Modeling ocean eddies on Antarctica's cold water continental shelves and their effects on ice shelf basal melting. Journal of Geophysical Research: Oceans, 124(7): 5067–5084, doi: 10.1029/2018jc014688

Malyarenko A, Robinson N J, Williams M J M, et al. 2019. A wedge mechanism for summer surface water inflow into the Ross Ice Shelf cavity. Journal of Geophysical Research: Oceans, 124(2): 1196–1214, doi: 10.1029/2018JC014594

Marshall J, Adcroft A, Hill C, et al. 1997a. A finite-volume, incompressible Navier Stokes model for studies of the ocean on parallel computers. Journal of Geophysical Research: Oceans, 102(C3): 5753–5766, doi: 10.1029/96JC02775

Marshall J, Hill C, Perelman L, et al. 1997b. Hydrostatic, quasi-hydrostatic, and nonhydrostatic ocean modeling. Journal of Geophysical Research: Oceans, 102(C3): 5733–5752, doi: 10.1029/96JC02776

Masumoto Y, Sasaki H, Kagimoto T, et al. 2004. A fifty-year eddy-resolving simulation of the world ocean-preliminary outcomes of OFES (OGCM for the Earth Simulator). Journal of the Earth Simulator, 1: 35–56, doi: 10.32131/jes.1.35

Matsuta T, Masumoto Y. 2023. Energetics of the Antarctic circumpolar current. Part I: the Lorenz energy cycle and the vertical energy redistribution. Journal of Physical Oceanography, 53(6): 1467–1484, doi: 10.1175/JPO-D-22-0133.1

Mazloff M R, Heimbach P, Wunsch C. 2010. An eddy-permit-

ting Southern Ocean state estimate. Journal of Physical Oceanography, 40(5): 880–899, doi: 10.1175/2009jpo4236.1

Menemenlis D, Campin J M, Heimbach P, et al. 2008. ECCO2: High resolution global ocean and sea ice data synthesis. Mercator Ocean Quarterly Newsletter, 31: 13–21

Olbers D, Willebrand J, Eden C. 2012. Ocean Dynamics. Berlin: Springer-Verlag, 199, doi: 10.1007/978-3-642-23450-7

Oort A H, Anderson L A, Peixoto J P. 1994. Estimates of the energy cycle of the oceans. Journal of Geophysical Research: Oceans, 99(C4): 7665–7688, doi: 10.1029/93JC03556

Oort A H, Peixóto J P. 1983. Global angular momentum and energy balance requirements from observations. Advances in Geophysics, 25: 355–490, doi: 10.1016/S0065-2687(08)60177-6

Padman L, Erofeeva S, Joughin I. 2003. Tides of the Ross Sea and Ross Ice Shelf cavity. Antarctic Science, 15(1): 31–40, doi: 10.1017/s0954102003001032

Padman L, Fricker H A, Coleman R, et al. 2002. A new tide model for the Antarctic ice shelves and seas. Annals of Glaciology, 34: 247–254, doi: 10.3189/172756402781817752

Padman L, Howard S L, Orsi A H, et al. 2009. Tides of the northwestern Ross Sea and their impact on dense outflows of Antarctic Bottom Water. Deep-Sea Research Part Ⅱ: Topical Studies in Oceanography, 56(13−14): 818–834, doi: 10.1016/j.dsr2.2008.10.026

Rack W, Price D, Haas C, et al. 2021. Sea ice thickness in the western Ross Sea. Geophysical Research Letters, 48(1): e2020GL090866, doi: 10.1029/2020GL090866

Rignot E, Jacobs S, Mouginot J, et al. 2013. Ice-shelf melting around Antarctica. Science, 341(6143): 266–270, doi: 10.1126/science.1235798

Roullet G, Capet X, Maze G. 2014. Global interior eddy available potential energy diagnosed from Argo floats. Geophysical Research Letters, 41(5): 1651–1656, doi: 10.1002/2013gl059004

Schaffer J, Timmermann R, Arndt J E, et al. 2016. A global, high-resolution data set of ice sheet topography, cavity geometry, and ocean bathymetry. Earth System Science Data, 8(2): 543–557, doi: 10.5194/essd-8-543-2016

Schodlok M P, Menemenlis D, Rignot E J. 2016. Ice shelf basal melt rates around Antarctica from simulations and observations. Journal of Geophysical Research: Oceans, 121(2): 1085–1109, doi: 10.1002/2015jc011117

Ssebandeke J, von Storch J S, Brüggemann N. 2024. Sensitivity of the Lorenz energy cycle of the global ocean. Ocean Dynamics, 74(1): 1–16, doi: 10.1007/s10236-023-01568-6

Stevens C, Hulbe C, Brewer M, et al. 2020. Ocean mixing and heat transport processes observed under the Ross Ice Shelf control its basal melting. Proceedings of the National Academy of Sciences of the United States of America, 117(29): 16799–16804, doi: 10.1073/pnas.1910760117

Sun Chong, Liu Chengyan, Wang Zhaomin, et al. 2022. On the influences of the continental shelf bathymetry correction in Prydz Bay, East Antarctica. Frontiers in Marine Science, 9: 957414, doi: 10.3389/fmars.2022.957414

Tailleux R. 2009. On the energetics of stratified turbulent mixing, irreversible thermodynamics, Boussinesq models and the ocean heat engine controversy. Journal of Fluid Mechanics, 638: 339–382, doi: 10.1017/S002211200999111X

Tailleux R. 2010. Entropy versus APE production: On the buoyancy power input in the oceans energy cycle. Geophysical Research Letters, 37(22): L22603, doi: 10.1029/2010GL044962

Tamura T, Ohshima K I. 2011. Mapping of sea ice production in the Arctic coastal polynyas. Journal of Geophysical Research: Oceans, 116(C7): C07030, doi: 10.1029/2010JC006586

Tamura T, Ohshima K I, Nihashi S, et al. 2011. Estimation of surface heat/salt fluxes associated with sea ice growth/melt in the Southern Ocean. SOLA, 7: 17–20, doi: 10.2151/sola.2011-005

Thompson L, Smith M, Thomson J, et al. 2020. Frazil ice growth and production during katabatic wind events in the Ross Sea, Antarctica. The Cryosphere, 14(10): 3329–3347, doi: 10.5194/tc-14-3329-2020

Verdy A, Mazloff M R. 2017. A data assimilating model for estimating Southern Ocean biogeochemistry. Journal of Geophysical Research: Oceans, 122(9): 6968–6988, doi: 10.1002/2016jc012650

von Storch J S, Eden C, Fast I, et al. 2012. An estimate of the Lorenz energy cycle for the world ocean based on the $1/10^{\circ}$ STORM/NCEP simulation. Journal of Physical Oceanography, 42(12): 2185–2205, doi: 10.1175/JPO-D-12-079.1

Wang Wei, Huang Ruixin. 2004. Wind energy input to the Ekman layer. Journal of Physical Oceanography, 34(5): 1267–1275, doi: 10.1175/1520-0485(2004)034<1267:WEITTE>2.0.CO;2

Wu Yang, Wang Zhaomin, Liu Chengyan. 2017. On the response of the Lorenz energy cycle for the Southern Ocean to intensified westerlies. Journal of Geophysical Research: Oceans, 122(3): 2465–2493, doi: 10.1002/2016JC012539

Wu Yang, Wang Zhaomin, Liu Chengyan. 2021. Impacts of changed ice-ocean stress on the North Atlantic Ocean: role of ocean surface currents. Frontiers in Marine Science, 8: 628892, doi: 10.3389/fmars.2021.628892

Wunsch C, Ferrari R. 2004. Vertical mixing, energy, and the general circulation of the oceans. Annual Review of Fluid Mechanics, 36: 281–314, doi: 10.1146/annurev.fluid.36.050802.122121

Yan Liangjun, Wang Zhaomin, Liu Chengyan, et al. 2023. The salinity budget of the Ross Sea continental shelf, Antarctica. Journal of Geophysical Research: Oceans, 128(3): e2022JC018979, doi: 10.1029/2022JC018979

Zhang Jinlun, Hibler III W D. 1997. On an efficient numerical method for modeling sea ice dynamics. Journal of Geophysical Research: Oceans, 102(C4): 8691–8702, doi: 10.1029/96jc03744

Zhang Jinlun, Rothrock D. 2000. Modeling Arctic sea ice with an efficient plastic solution. Journal of Geophysical Research: Oceans, 105(C2): 3325–3338, doi: 10.1029/1999jc900320

Zhang Yimin, Yang Wei, Zhao Wei, et al. 2023. Spatial and seasonal variations of near-inertial kinetic energy in the upper Ross Sea and the controlling factors. Frontiers in Marine Science, 10: 1173900, doi: 10.3389/fmars.2023.1173900

Zweng M M, Reagan J R, Seidov D, et al. 2019. World Ocean Atlas 2018, volume 2: Salinity. A. Mishonov, ed. Silver Spring, MD, USA: NOAA Atlas NESDIS 82, 50, https://archimer.ifremer.fr/doc/00651/76339/77330.pdf [2019-07-01]

Supplementary information:

Fig. S1. Location of observation sites. The dots with color shading show the location of observation sites from the MEOP. Color coding denotes the seasons of the spring (September, October, and November), the summer (December, January, and February), the autumn (March, April, and May), and the winter (June, July, and August). The two yellow lines represent the locations of two selected cross-sections (165°E and 175°E). The yellow and red triangles are the location of mooring sites (CA107, 71.46°S, 172.30°E; CA208, 71.42°S, 172.38°E) from the CALM. The black triangle denotes the location of a coastal mooring site (C1, 74.59°S, 165.23°E) provided by the Zhejiang University.

Fig. S2. Comparisons of the salinity (the upper row), potential temperature (the middle row), and potential density (the lower row) between model results (the left column), MEOP data (the middle column), and the differences (the right column, model minus observation) at the 165°E cross-section (the western yellow line in Fig. S1) in spring. RMSE denotes the Root Mean Square Error between model result of observations.

Fig. S3. Comparisons of the salinity (the upper row), potential temperature (the middle row), and potential density (the lower row) between model results (the left column), MEOP data (the middle column), and the differences (the right column, model minus observation) at the 165°E cross-section (the western yellow line in Fig. S1) in summer. RMSE denotes the Root Mean Square Error between model result of observations.

Fig. S4. Comparisons of the salinity (the upper row), potential temperature (the middle row), and potential density (the lower row) between model results (the left column), MEOP data (the middle column), and the differences (the right column, model minus observation) at the 165°E cross-section (the western yellow line in Fig. S1) in autumn. RMSE denotes the Root Mean Square Error between model result of observations.

Fig. S5. Comparisons of the salinity (the upper row), potential temperature (the middle row), and potential density (the lower row) between model results (the left column), MEOP data (the middle column), and the differences (the right column, model minus observation) at the 165°E cross-section (the western yellow line in Fig. S1) in winter. RMSE denotes the Root Mean Square Error between model result of observations.

Fig. S6. Comparisons of the salinity (the upper row), potential temperature (the middle row), and potential density (the lower row) between model results (the left column), MEOP data (the middle column), and the differences (the right column, model minus observation) at the 175°E cross-section (the eastern yellow line in Fig. S1) in spring.

Fig. S7. Comparisons of the salinity (the upper row), potential temperature (the middle row), and potential density (the lower row) between model results (the left column), MEOP data (the middle column), and the differences (the right column, model minus observation) at the 175°E cross-section (the eastern yellow line in Fig. S1) in summer.

Fig. S8. Comparisons of the salinity (the upper row), potential temperature (the middle row), and potential density (the lower row) between model results (the left column), MEOP data (the middle column), and the differences (the right column, model minus observation) at the 175°E cross-section (the eastern yellow line in Fig. S1) in autumn.

Fig. S9. Comparisons of the salinity (the upper row), potential temperature (the middle row), and potential density (the lower row) between model results (the left column), MEOP data (the middle column), and the differences (the right column, model minus observation) at the 175°E cross-section (the eastern yellow line in Fig. S1) in winter.

Fig. S10. Comparisons of the salinity (the upper row), potential temperature (the middle row), and potential density (the lower row) between model results (the left column) and MEOP data (the middle column), and the differences (the right column, model results minus observational values) at 100 m depth in spring.

Fig. S11. Comparisons of the salinity (the upper row), potential temperature (the middle row), and potential density (the lower row) between model results (the left column) and MEOP data (the middle column), and the differences (the right column, model results minus observational values) at 100 m depth in summer.

Fig. S12. Comparisons of the salinity (the upper row), potential temperature (the middle row), and potential density (the lower row) between model results (the left column) and MEOP data (the middle column), and the differences (the right column, model results minus observational values) at 100 m depth in autumn.

Fig. S13. Comparisons of the salinity (the upper row), potential temperature (the middle row), and potential density (the lower

row) between model results (the left column) and MEOP data (the middle column), and the differences (the right column, model results minus observational values) at 100 m depth in winter.

Fig. S14. Comparisons of the salinity (the upper row), potential temperature (the middle row), and potential density (the lower row) between model results (the left column) and MEOP data (the middle column), and the differences (the right column, model results minus observational values) at 215 m depth in spring.

Fig. S15. Comparisons of the salinity (the upper row), potential temperature (the middle row), and potential density (the lower row) between model results (the left column) and MEOP data (the middle column), and the differences (the right column, model results minus observational values) at 215 m depth in summer.

Fig. S16. Comparisons of the salinity (the upper row), potential temperature (the middle row), and potential density (the lower row) between model results (the left column) and MEOP data (the middle column), and the differences (the right column, model results minus observational values) at 215 m depth in autumn.

Fig. S17. Comparisons of the salinity (the upper row), potential temperature (the middle row), and potential density (the lower row) between model results (the left column) and MEOP data (the middle column), and the differences (the right column, model results minus observational values) at 215 m depth in winter.

Fig. S18. Spearman correlation analysis between model results and observations from MEOP at the 165°E cross-section. Scatter colors denote the depths at which θ and S data pairs were collected. a and b. Comparison of θ and S in spring, respectively. c and d. Comparison of θ and S in summer, respectively. e and f. Comparison of θ and S in autumn, respectively. g and h. Comparison of θ and S in winter, respectively.

Fig. S19. Spearman correlation analysis between model results and observations from MEOP at the 175°E cross-section. Scatter colors denote the depths at which θ and S data pairs were collected. a and b. Comparison of θ and S in spring, respectively. c and d. Comparison of θ and S in summer, respectively. e and f. Comparison of θ and S in autumn, respectively. g and h. Comparison of θ and S in winter, respectively.

Fig. S20. Spearman correlation analysis between model results and observations at 100 m depths. Scatter colors denote the depths at which θ and S data pairs were collected. a and b. Comparison of θ and S in spring, respectively. c and d. Comparison of θ and S in summer, respectively. e and f. Comparison of θ and S in autumn, respectively. g and h. Comparison of θ and S in winter, respectively.

Fig. S21. Spearman correlation analysis between model results and observations at 215 m depths. Scatter colors denote the depths at which θ and S data pairs were collected. a and b. Comparison of θ and S in spring, respectively. c and d. Comparison of θ and S in summer, respectively. e and f. Comparison of θ and S in autumn, respectively. g and h. Comparison of θ and S in winter, respectively.

Fig. S22. Comparisons of S between model results (red lines) and mooring observations (cyan lines) at various depths. The mooring position is shown by the black triangle in Fig. S1.

Fig. S23. Comparisons of θ between model results (red lines) and mooring observations (cyan lines) at various depths. The mooring position is shown by the black triangle in Fig. S1.

Fig. S24. Comparison of the velocity magnitude between model results and observations. a. Time series at the CA107 site (the yellow triangle in Fig. S1) and the model outputs. b. Time series at the CA208 site (the red triangle in Fig. S1) and the model outputs.

Fig. S25. Comparisons of the sea ice concentration between model results and satellite observations from the University Bremen. a and c. The sea ice concentration from the model results in the austral summer and in the austral winter, respectively. b and d. The sea ice concentration from the satellite observations from the University Bremen in the austral summer and in the austral winter, respectively. c and f. The differences in the sea ice concentration between model results and observations in summer (model results minus observations) in the austral summer and in the austral winter, respectively.

Fig. S26. Distribution of the simulated time-mean buoyancy flux.

Fig. S27. Distribution of the simulated time-mean buoyancy flux in the sub-ice-shelf cavity.

Fig. S28. Time-mean velocity of the surface layer. The color shading indicates the magnitude of current velocities. Black arrows denote the current velocity vectors.

Fig. S29. Distribution of wind vectors. The color shading indicates the magnitude of the wind velocity. Black arrows denote the wind velocity vectors.

Fig. S30. Distribution of the simulated first baroclinic Rossby deformation radius.

Fig. S31. Distribution of freshwater flux. Positive values represent increased salinity.

Fig. S32. Distribution of freshwater flux. Positive values represent increased salinity, but for the sub-ice-shelf cavity.

Fig. S33. Distribution of heat flux. Positive values represent ocean lose heat.

Fig. S34. Distribution of heat flux. Positive values represent ocean lose heat, but for the sub-ice-shelf cavity.

Fig. S35. Distribution of ρ^*.

Fig. S36. Distribution of ρ^*, but for the sub-ice-shelf cavity.

The supplementary information is available online at https://doi.org/10.1007/s13131-025-2478-0 and http://www.aosocean.com/. The supplementary information is published as submitted, without typesetting or editing. The responsibility for scientific accuracy and content remains entirely with the authors.